Subsynchronous Oscillation Mechanism and Its Suppression in MMC-Based HVDC Connected Wind Farms

Article *in* IET Generation Transmission & Distribution · October 2017

DOI: 10.1049/iet-gtd.2017.1066

4 authors, including:

Jing Lyu
Norwegian University of Science and Technol…
19 PUBLICATIONS **63** CITATIONS
SEE PROFILE

Mohammad Amin
Illinois Institute of Technology
27 PUBLICATIONS **109** CITATIONS
SEE PROFILE

Marta Molinas
Norwegian University of Science and Technol…
292 PUBLICATIONS **3,187** CITATIONS
SEE PROFILE

Subsynchronous Oscillation Mechanism and Its Suppression in MMC-Based HVDC Connected Wind Farms

Jing Lyu [1,2*], Xu Cai [1], Mohammad Amin[2], Marta Molinas[2]

[1] Wind Power Research Centre, Shanghai Jiao Tong University, Shanghai, China
[2] Department of Engineering Cybernetics, Norwegian University of Science and Technology, Trondheim, Norway
[*]jing.lyu@ntnu.no

Abstract: A subsynchronous oscillation (SSO) phenomenon in a wind farm integrated with a modular multilevel converter (MMC)-based high-voltage direct current (HVDC) transmission system has been recently observed in the real world. An attempt is made in this paper to contribute to the understanding of the root cause of the SSO in the MMC-HVDC connected wind farms by the impedance-based analysis. For that, the small-signal impedance model of the MMC is first developed based on the harmonic state-space (HSS) modelling method, which is able to include all the internal harmonic dynamics of MMC. An inherent low-frequency resonance peak in the MMC system excluding any control influence is identified by its terminal impedance characteristics. Arguably, this could be the reason why the SSO phenomenon occurs in the MMC-HVDC connected wind farms. In addition to that, the influence factors, such as main circuit parameters, controller parameters, and power level, on the stability of the interconnected system are examined by the impedance-based Nyquist plots, which can provide guidelines for the system design in order to guarantee the stability of the interconnected system. Based on the mechanism analysis, a stabilization control method for suppressing the SSO in the MMC-HVDC based wind farms is also proposed. Finally, the theoretical analysis and stabilization control method are validated by both time-domain simulations and on-site recorded waveforms in a real MMC-HVDC system for wind farm integration in China.

1. Introduction

Offshore wind power is the development trend of wind power generation. In future, offshore wind farms will have large capacity and will be situated much farther offshore than current projects [1]. An important issue is how to deliver the electricity from offshore to onshore. It has been well accepted that high-voltage direct current (HVDC) transmission technology, especially voltage-source converter based HVDC (VSC-HVDC) technology, will become an attractive and feasible option for grid integration of large-scale offshore wind farms [2, 3]. Among the different techniques of HVDC converters, the modular multilevel converter (MMC) is regarded as a promising solution for high-voltage/high-power applications due to its advantages, such as high modularity, low switching loss, low distortion of output voltage, decoupling control of active and reactive power, and so forth [4, 5].

However, compared with conventional VSCs, MMCs have much more complex internal dynamics [6-8], such as harmonic circulating currents and capacitor voltage fluctuations, which might have detrimental effects on the operation stability of the interconnected system, especially for renewable energy integration applications [9-11]. For instance, a subsynchronous oscillation (SSO) phenomenon was observed in a real MMC-HVDC project for wind farm integration in China [10], where the oscillation frequency is approximately 21 Hz in the ac phase currents (as shown in Fig. 8*a*). Furthermore, it is worth noting that there are several different types of wind farms in the project, including fixed speed induction generator (FSIG) based wind farm, doubly-fed induction generator (DFIG) based wind farm, and permanent magnet synchronous generator (PMSG) based wind farm, and a similar oscillatory phenomenon appeared when each type of wind farm was separately connected to the MMC-HVDC transmission system.

Several papers have so far discussed the stability of MMC-HVDC connected wind farms [9-14]. The SSO phenomenon in the MMC-HVDC system with wind farms was reported in [9, 10], in which the propagation mechanism of the SSO current in the MMC-HVDC system was investigated. The frequency-domain stability analysis of the MMC-HVDC system for wind farm integration was carried out by using the impedance-based approach in [11, 12], where the ac-side small-signal impedance models of the MMC were developed. What distinguishes this paper from the above contributions is the elucidation of the SSO generation mechanism, which this paper discusses in depth in the light of a high fidelity modelling that includes: the capacitor voltage harmonics, dc and high-order harmonic circulating currents, which were ignored in the MMC impedance modelling in the previous papers. The stabilization control methods for enhancing the stability of the MMC-HVDC based wind farms were investigated in [13], whereas the factors that influence the stability of the interconnected system were not discussed. Additionally, the small-signal stability of synchronverter based wind farm with MMC-HVDC was investigated in [14], which shows the synchronverter's superiority in grid-integration stability in comparison to the PLL-based dq-domain current control, but again the paper merely focused on the control and stability mechanism of the wind power inverter while neglecting the MMC internal dynamics. In addition, the high-frequency resonance issues caused by the distributed capacitance of the long transmission cables [15], the parallel

This article has been accepted for publication in a future issue of this journal, but has not been fully edited.
Content may change prior to final publication in an issue of the journal. To cite the paper please use the doi provided on the Digital Library page.

resonance in wind farms caused by the shunt capacitor banks and high-frequency harmonic filters [16], and the subsynchronous resonance in DFIG-based wind farms caused by the series-compensated capacitors [17] were also investigated. However, the instability mechanisms above mainly depend on the physical LC resonance configuration, which could not provide deep insight into the unique SSO phenomenon in the MMC-HVDC system with wind farms. The small-signal stability of a wind farm connected to a VSC-HVDC system was discussed in [18, 19], in which, however, the VSC-HVDC system is based on two-level converters that lack the internal dynamics. Therefore, this instability mechanism would still not be able to correctly interpret the SSO phenomenon in the MMC-HVDC connected wind farms.

An attempt is made in this paper to contribute to the understanding of the root cause of the SSO phenomenon in the MMC-HVDC based wind farms, based on a high fidelity modelling. Furthermore, the influence factors, such as main circuit parameters, controller parameters and power transfer level, on the stability of the interconnected system will be further examined in order to provide guidelines for system design to enhance the stability of the interconnected system. The impedance-based analytical approach is adopted in this work. For that, the ac-side small-signal impedance model of the MMC is developed based on the harmonic state-space modelling method, which is able to include all the internal harmonic dynamics within MMC. Subsequently, the generation mechanism of the SSO phenomenon in the MMC-HVDC connected wind farms is revealed from an impedance characteristic perspective. Based on the mechanism analysis, a stabilization control method is also proposed to suppress the SSO in the MMC-HVDC based wind farms. Finally, time-domain simulations and on-site recorded waveforms validate the theoretical analysis and stabilization control method.

2. System description

Fig. 1*a* shows the overall diagram of the MMC-HVDC connected wind farm, where the wind farm consists of full-power wind turbines based on two-level VSCs, and the MMC-HVDC system comprises a wind farm side MMC station (WFMMC) and a grid side MMC station (GSMMC).

For simplicity, the wind farm is modelled by an aggregated wind turbine generator, where the generator side dynamics are ignored since they have less impact on the grid side dynamics [18, 19]. Furthermore, it is assumed that the ac power grid is strong and the control bandwidth of the dc voltage loop of the GSMMC is less than the SSO frequency under study, which means that the dc voltage control dynamic of the GSMMC has little effect on the ac-side dynamics of the WFMMC. Hence, the GSMMC can be simply replaced with a dc voltage source. The simplified circuit diagram of the interconnected system is presented in Fig. 1*b*, where T1 is the converter transformer of the WFMMC, T2 is the step-up transformer of the wind farm, T3 is the aggregated step-up transformer of the wind turbine, and L_w is the aggregated ac filter inductance of the wind turbine. The conventional *dq*-domain current control with PLL [13, 18] is used in the wind power inverter, and the ac voltage control in the stationary *abc* frame [11, 13] is employed in the WFMMC.

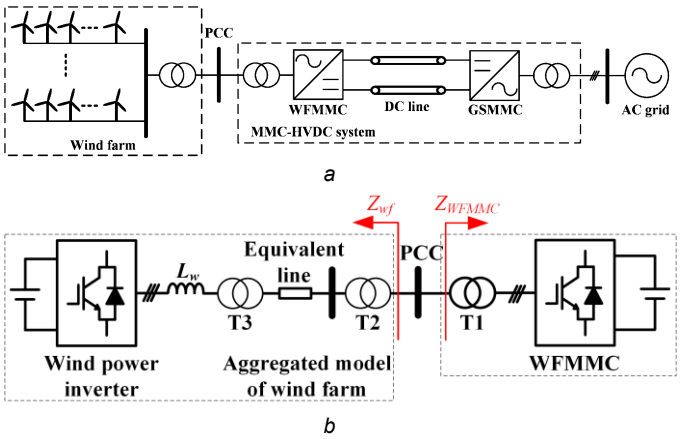

Fig. 1. *Configuration diagram of wind farm integration via an MMC-HVDC transmission system*
a Overall structure
b Simplified system under study

3. Harmonic state-space (HSS) modelling of MMC

3.1. Formulation of HSS modelling

For any time-varying periodic signal $x(t)$, it can be written in the form of Fourier series as:

$$x(t)=\sum_{k\in\mathbb{Z}} X_k e^{jk\omega_1 t} \tag{1}$$

where $\omega_1=2\pi/T$, T is the fundamental period of the signal, and X_k is the Fourier coefficient that can be calculated by

$$X_k=\frac{1}{T}\int_{t_0}^{t_0+T} x(t)e^{-jk\omega_1 t}dt \tag{2}$$

The state-space equation of a linear time periodic (LTP) system can be expressed as

$$\dot{x}(t)=A(t)x(t)+B(t)u(t) \tag{3}$$

Based on the Fourier series and harmonic balance theory [20, 21], the state-space equation in time-domain can be transformed into the harmonic state-space equation in frequency-domain, which is like

$$s\mathbf{X}=(\mathbf{A}-\mathbf{Q})\mathbf{X}+\mathbf{B}\mathbf{U} \tag{4}$$

where **X**, **U**, **Q,** and **A** are indicated as (5)~(8), respectively, **B** is the same form as **A**. The elements X_h, U_h, and A_h are the Fourier coefficient of the hth harmonic of $x(t)$, $u(t)$, and $A(t)$ in (3), respectively. Note that **A** and **B** are Toeplitz matrices in order to perform the frequency-domain convolution operation, **Q** is a diagonal matrix that represents the frequency information, and I is an identity matrix having the same matrix size with the number of state variables. In addition, it should be noted that the harmonic order h considered in the model needs to be selected according to the requirements for accuracy and complexity of the model.

$$\mathbf{X}=\left[X_{-h},\cdots,X_{-1},X_0,X_1,\cdots,X_h\right]^T \tag{5}$$

$$\mathbf{U}=\left[U_{-h},\cdots,U_{-1},U_0,U_1,\cdots,U_h\right]^T \tag{6}$$

$$\mathbf{Q}=\mathrm{diag}\left[-jh\omega_1\bullet I,\cdots,0\bullet I,\cdots,jh\omega_1\bullet I\right] \tag{7}$$

$$\mathbf{A}=\begin{bmatrix} A_0 & A_{-1} & \cdots & A_{-h} & & & \\ A_1 & \ddots & \ddots & \ddots & \ddots & & \\ \vdots & \ddots & A_0 & A_{-1} & \ddots & \ddots & \\ A_h & \ddots & A_1 & A_0 & A_{-1} & \ddots & A_{-h} \\ & \ddots & \ddots & A_1 & A_0 & \ddots & \vdots \\ & & \ddots & \ddots & \ddots & \ddots & A_{-1} \\ & & & A_h & \cdots & A_1 & A_0 \end{bmatrix} \tag{8}$$

3.2. HSS modelling of MMC

It is assumed that the equivalent switching frequency is high enough and the capacitor voltages are balanced at all times [6-8]. Hence, the averaged equivalent circuit of MMC can be obtained, as presented in Fig. 2 (taking one phase for example), where C_{arm}=C_{SM}/N, C_{SM} is the submodule (SM) capacitance, N is SM number per arm, L and R are the arm inductance and equivalent series resistance, respectively, i_u and i_l are the upper and lower arm currents, respectively, v_{cu}^{Σ} and v_{cl}^{Σ} are the sum capacitor voltages of the upper and lower arms, respectively, v_g and i_g are the ac-side phase voltage and current, respectively, i_c is the circulating current, V_{dc} is the dc bus voltage, and n_u and n_l are the switching functions of the upper and lower arms, respectively. In addition, Z_L(=R_L+$j\omega_1 L_L$) is the ac-side equivalent load in order to determine the steady-state operating point, and v_p is the injected small perturbation voltage in order to develop the small-signal impedance of MMC according to the harmonic linearization theory. Furthermore, the dc-link voltage V_{dc} is assumed to be constant.

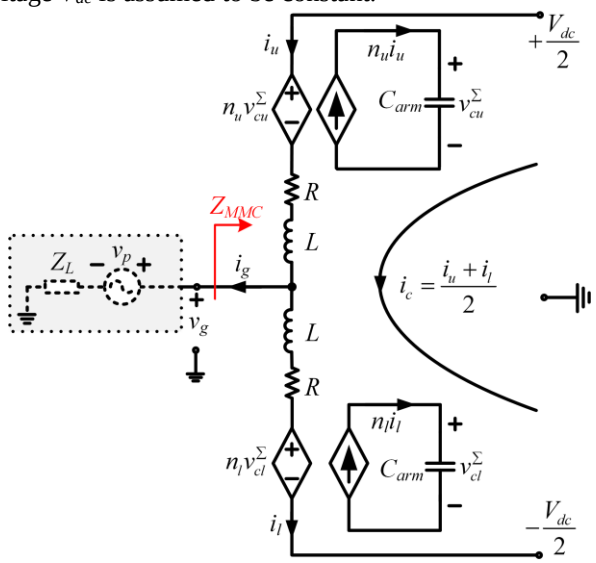

Fig. 2. *Averaged equivalent circuit of one phase leg of MMC*

According to Fig. 2, the time-domain state-space equation of one phase leg of MMC can be expressed as (3), where $x(t)$, $u(t)$, $A(t)$, and $B(t)$ are shown in (9)~(12).

$$x(t)=\left[i_c, v_{cu}^{\Sigma}, v_{cl}^{\Sigma}, i_g\right]^T \tag{9}$$

$$u(t)=\left[V_{dc}\right] \tag{10}$$

$$A(t)=\begin{bmatrix} -\frac{R}{L} & -\frac{n_u}{2L} & -\frac{n_l}{2L} & 0 \\ \frac{n_u}{C_{arm}} & 0 & 0 & \frac{n_u}{2C_{arm}} \\ \frac{n_l}{C_{arm}} & 0 & 0 & -\frac{n_l}{2C_{arm}} \\ 0 & -\frac{n_u}{L} & \frac{n_l}{L} & -\frac{R+2Z_L}{L} \end{bmatrix} \tag{11}$$

$$B(t)=\left[\frac{1}{2L},0,0,0\right]^T \tag{12}$$

where the switching functions n_u and n_l are determined by the controller employed in the MMC (e.g., the ac voltage controller in this paper), which can be expressed as

$$\begin{cases} n_u=\frac{1}{2}\left[1-m\cos\left(\omega_1 t+\theta_{m1}\right)\right] \\ n_l=\frac{1}{2}\left[1+m\cos\left(\omega_1 t+\theta_{m1}\right)\right] \end{cases} \tag{13}$$

in which m and θ_{m1} are the modulation index and phase of the modulation reference voltage, respectively.

It is noted that there are significant steady-state harmonic components in the state variables such as i_c, v_{cu}^{Σ}, and v_{cl}^{Σ}, which are caused by the operation characteristics of MMC. For instance, the circulating current i_c mainly contains dc and second harmonic components as well as other even harmonics which are negligibly small in normal operation. Moreover, the capacitor voltages v_{cu}^{Σ} and v_{cl}^{Σ} theoretically contain all the harmonics, in which, however, the dc, fundamental, second and third harmonic components are dominant in normal cases. Therefore, in order to obtain an accurate MMC model, the HSS modelling method, in which harmonics of state variables, inputs, and outputs are posed separately in a state-space form, is introduced to model the MMC in this work.

By using the HSS modelling procedure to the MMC that is formulated as (3), the HSS model of MMC can be obtained as (4), where the elements X_h, U_h, A_h, and B_h are shown in (14)~(17). O is zero matrix.

$$X_{\pm h}=\left[I_{c\pm h}, V_{cu\pm h}^{\Sigma}, V_{cl\pm h}^{\Sigma}, I_{g\pm h}\right] \tag{14}$$

$$U_0=\left[V_{dc}\right], U_{\pm h}=\left[0\right]\left(h\geq 1\right) \tag{15}$$

$$A_0=\begin{bmatrix} -\frac{R}{L} & -\frac{1}{4L} & -\frac{1}{4L} & 0 \\ \frac{1}{2C_{arm}} & 0 & 0 & \frac{1}{4C_{arm}} \\ \frac{1}{2C_{arm}} & 0 & 0 & -\frac{1}{4C_{arm}} \\ 0 & -\frac{1}{2L} & \frac{1}{2L} & -\frac{R+2Z_L}{L} \end{bmatrix} \tag{16a}$$

$$A_{\pm 1}=\begin{bmatrix} 0 & \frac{me^{\pm j\theta_{m1}}}{8L} & -\frac{me^{\pm j\theta_{m1}}}{8L} & 0 \\ -\frac{me^{\pm j\theta_{m1}}}{4C_{arm}} & 0 & 0 & -\frac{me^{\pm j\theta_{m1}}}{8C_{arm}} \\ \frac{me^{\pm j\theta_{m1}}}{4C_{arm}} & 0 & 0 & -\frac{me^{\pm j\theta_{m1}}}{8C_{arm}} \\ 0 & \frac{me^{\pm j\theta_{m1}}}{4L} & \frac{me^{\pm j\theta_{m1}}}{4L} & 0 \end{bmatrix} \tag{16b}$$

$$A_{\pm h}=O^{4\times 4}\left(h\geq 2\right) \tag{16c}$$

$$B_0=\left[\frac{1}{2L},0,0,0\right]^T \tag{17a}$$

$$B_{\pm h}=O^{4\times 1}\left(h\geq 1\right) \tag{17b}$$

Letting the left side of (4) to be zero, the steady-state harmonic components of state variables can thus be calculated by

$$\mathbf{X}_{ss}=-\left(\mathbf{A}-\mathbf{Q}\right)^{-1}\mathbf{B}\mathbf{U} \tag{18}$$

4. Impedance modelling of the interconnected system

4.1. Impedance modelling of WFMMC

According to the harmonic linearization principle [22], by injecting a small sinusoidal perturbation voltage in the ac-side of the MMC (as shown in Fig. 2) and then calculating the corresponding current response of the MMC at the perturbation frequency, the ac-side small-signal impedance can thus be obtained by calculating the ratio of the resulting complex voltage to current at the perturbation frequency, which is defined as

$$Z_{MMC}\left(j\omega_p\right)=-\frac{\boldsymbol{v}_{gp}}{\boldsymbol{i}_{gp}} \tag{19}$$

where the bold letters $\boldsymbol{v}_{gp}$ and $\boldsymbol{i}_{gp}$ represent the complex phasors of small perturbations $v_{gp}(t)$ and $i_{gp}(t)$ at frequency ω_p, respectively.

According to the operation principle of MMC, the injected small perturbation voltage will lead to perturbations in all variables at frequencies that are listed as follows:

$$\omega_p,\omega_p\pm\omega_1,\omega_p\pm2\omega_1,\cdots,\omega_p\pm h\omega_1 \tag{20}$$

Applying small perturbation analysis to the state-space equation of the MMC formulated in (3) and (9)~(12), the small perturbation state-space equation of the MMC can be expressed as

$$\dot{x}_p\left(t\right)=A_p\left(t\right)x_p\left(t\right)+B_p\left(t\right)u_p\left(t\right) \tag{21}$$

where $x_p\left(t\right)=\left[i_{cp},v_{cup}^{\Sigma},v_{clp}^{\Sigma},i_{gp}\right]^T$, $u_p\left(t\right)=\left[n_{up},n_{lp},v_p\right]^T$, $A_p(t)$ and $B_p(t)$ are given in (22) and (23), respectively. The subscripts "p" and "s" denote perturbation and steady-state components, respectively.

$$A_p\left(t\right)=\begin{bmatrix}-\frac{R}{L} & -\frac{n_{us}}{2L} & -\frac{n_{ls}}{2L} & 0\\ \frac{n_{us}}{C_{arm}} & 0 & 0 & \frac{n_{us}}{2C_{arm}}\\ \frac{n_{ls}}{C_{arm}} & 0 & 0 & -\frac{n_{ls}}{2C_{arm}}\\ 0 & -\frac{n_{us}}{L} & \frac{n_{ls}}{L} & -\frac{R+2Z_L}{L}\end{bmatrix} \tag{22}$$

$$B_p\left(t\right)=\begin{bmatrix}-\frac{v_{cus}^{\Sigma}}{2L} & -\frac{v_{cls}^{\Sigma}}{2L} & 0\\ \frac{1}{C_{arm}}\left(i_{cs}+\frac{i_{gs}}{2}\right) & 0 & 0\\ 0 & \frac{1}{C_{arm}}\left(i_{cs}-\frac{i_{gs}}{2}\right) & 0\\ -\frac{v_{cus}^{\Sigma}}{L} & \frac{v_{cls}^{\Sigma}}{L} & -\frac{2}{L}\end{bmatrix} \tag{23}$$

In addition, the small perturbations n_{up} and n_{lp} of the switching functions are determined by the ac voltage controller used in the WFMMC, which can be obtained as

$$\begin{cases}\boldsymbol{n}_{up}=-\frac{k_f-H_v}{V_{dc}}\boldsymbol{v}_{gp}\triangleq-G_v\boldsymbol{v}_{gp}\\ \boldsymbol{n}_{lp}=\frac{k_f-H_v}{V_{dc}}\boldsymbol{v}_{gp}\triangleq G_v\boldsymbol{v}_{gp}\end{cases} \tag{24}$$

where H_v is the ac voltage regulator and k_f is the voltage feed-forward gain [13]. Additionally, the small perturbation $\boldsymbol{v}_{gp}$ can be expressed as

$$\boldsymbol{v}_{gp}=\boldsymbol{v}_p+Z_L\boldsymbol{i}_{gp} \tag{25}$$

Hence, according to (21)~(25), the small perturbation HSS model of the MMC can be obtained as (26) by applying the HSS modelling procedure that is introduced in (1)~(8).

$$s\mathbf{X}_p=\left(\mathbf{A}_p-\mathbf{Q}_p\right)\mathbf{X}_p+\mathbf{B}_p\mathbf{U}_p \tag{26}$$

where $\mathbf{X}_p$, $\mathbf{U}_p$, and $\mathbf{Q}_p$ are given as (27)~(29), in which the subscript "$p\pm h$" denotes the perturbation component at frequency "$\omega_p\pm h\omega_1$". Additionally, the elements of $\mathbf{A}_p$ and $\mathbf{B}_p$ are shown in Appendix (A1)~(A5).

$$\begin{aligned}\mathbf{X}_p&=\left[X_{p-h},\cdots,X_p,\cdots,X_{p+h}\right]^T\\ X_{p\pm h}&=\left[I_{cp\pm h},V_{cup\pm h}^{\Sigma},V_{clp\pm h}^{\Sigma},I_{gp\pm h}\right]\end{aligned} \tag{27}$$

$$\begin{aligned}\mathbf{U}_p&=\left[U_{p-h},\cdots,U_p,\cdots,U_{p+h}\right]^T\\ U_p&=\left[V_p\right],U_{p\pm h}=\left[0\right]\left(h\geq1\right)\end{aligned} \tag{28}$$

$$\mathbf{Q}_p=\mathrm{diag}\left[j\left(\omega_p-h\omega_1\right)\bullet I,\ldots,j\omega_p\bullet I,\ldots,j\left(\omega_p+h\omega_1\right)\bullet I\right] \tag{29}$$

By ignoring the transient behavior of the perturbation signals, that is, letting the left-hand side of (26) to be zero, the perturbation components of the state variables at each perturbation frequency defined in (20) can thus be calculated by

$$\mathbf{X}_p=-\left(\mathbf{A}_p-\mathbf{Q}_p\right)^{-1}\mathbf{B}_p\mathbf{U}_p \tag{30}$$

According to the definition of the small-signal impedance in (19), only the resulting perturbation voltage and current at frequency ω_p in the ac-side of the MMC need to be concerned. In order to solve (30), the harmonic order h must be predetermined. From (30), the perturbation current $\boldsymbol{i}_{gp}$ at frequency ω_p (i.e., I_{gp} in eq. (27)) can be calculated. Subsequently, the perturbation voltage $\boldsymbol{v}_{gp}$ at frequency ω_p can be readily figured out by substituting $\boldsymbol{i}_{gp}$ in (25). Hence, the ac-side small-signal impedance of the MMC at frequency ω_p can be calculated by (19). Finally, the WFMMC impedance Z_{WFMMC} can be obtained by adding the converter transformer impedance and the MMC impedance which needs to be converted to the PCC side of the converter transformer.

4.2. Impedance model verification

To verify the derived impedance models of the MMC, a time-domain simulation model of a three-phase MMC with a three-phase passive load is built in MATLAB/Simulink. In the simulation, the ac-side small-signal impedances of the MMC are measured by means of injecting a series of small perturbation voltage signals at different frequencies with the interval of 1 Hz in the ac-side of the MMC. Then by measuring the resulting perturbation currents, the ac-side small-signal impedances can be easily calculated for each frequency. The main electrical parameters of the MMC are as follows: the fundamental frequency 50 Hz, converter-side voltage 166 kV, dc-link voltage 320 kV, SM number per arm 20, SM capacitance 140 μF, arm inductance 360 mH. It is noted that the main electrical parameters of the MMC used in this paper are identical to those of the real system, but both the SM number and capacitance are one-tenth of the actual parameters, where keeping the arm equivalent capacitance C_{arm} unchanged.

Fig. 3*a* shows the comparison between the analytical and

measured ac-side small-signal impedances of the MMC with ac voltage closed-loop control, where the harmonic order *h* of the analytical model is selected as 4. It is seen that the analytical impedance matches well with the measured one, which validates the analytical impedance model. Moreover, this paper mainly focuses on the ac-side impedance characteristics of the MMC within 200 Hz frequency range, since the impedance characteristics above 200 Hz, which are primarily determined by the arm inductance, are inductive.

In order to uncover the impact of the inherent dynamics on the MMC impedance, the ac-side impedance of the MMC with open-loop control is also presented in this paper, as shown in Fig. 3*b*. By comparing Fig. 3*b* with Fig. 3*a*, it can be observed that both of them have a similar shape, where the major difference is at the fundamental frequency (50 Hz hereof) because of the integral part of the ac voltage controller. Furthermore, it can be seen that there are several resonance points in the ac-side impedance of the MMC below 200 Hz even without any control influence, which are originated from the internal dynamics of the MMC.

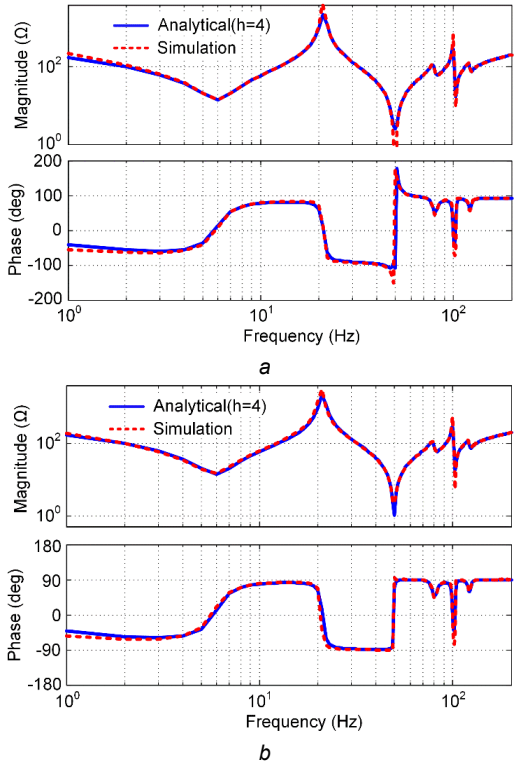

Fig. 3. *Validation for the ac-side small impedance model of the MMC*
a With ac voltage closed-loop control
b With open-loop control

4.3. Impedance modelling of wind farm

The key point of the impedance modelling of the wind farm is the impedance modelling of the wind power inverter. Since PLL-based grid synchronization is used in the wind power inverter, the impact of PLL on the ac-side impedance of the wind power inverter has to be considered. Furthermore, the positive- and negative-sequence impedances of the wind power inverter are not the same because of the *dq*-domain current control with PLL dynamics used in the wind power inverter. However, it is worth noting that the negative-sequence subsystem is more stable than the positive-sequence subsystem in a balanced positive-sequence interconnected system [18]. Therefore, in order to simplify the stability analysis, the negative-sequence subsystem is omitted in this paper. The sequence impedances of two-level VSCs with *dq*-domain current control and PLL dynamics have been derived in [23], which will not be further discussed in this paper. The wind farm impedance Z_{wf} includes the wind power inverter impedance, step-up transformer impedances and collection line impedance. However, the collection line impedance, which has little impact on the SSO phenomenon under study, is omitted in this paper, due to its short distance and high-frequency characteristics.

5. SSO mechanism, influence factors analysis, and stabilization control

5.1. SSO mechanism in MMC-HVDC connected wind farms

According to the impedance-based stability criterion [24], if the wind farm and WFMMC are stable separately, the stability of the interconnected system is determined by the impedance ratio (also called as minor-loop gain), which is given by

$$T_m(s) = \frac{Z_{WFMMC}(s)}{Z_{wf}(s)} \tag{31}$$

Fig. 4 shows the ac-side impedance-frequency characteristics of the WFMMC and wind farm under different power level conditions, i.e. 10%, 20%, and 40% of the rated power. It is seen that the magnitude of the wind farm impedance decreases as the output active power of the wind farm increases, while the phase of the wind farm impedance is almost unchanged. Furthermore, the WFMMC impedance is basically unrelated to the wind farm output power level. It is worth noting that the magnitude-frequency characteristics of the WFMMC and wind farm impedances intersect around the low-frequency resonance peak of the WFMMC impedance where the corresponding phase margin (PM) of the interconnected system becomes small or even less than zero as the output power of the wind farm becomes large, e.g., 20% power level with phase margin of about 20 °, and 40% power level with phase margin of about 7 ° which indicates that the interconnected system is marginally stable and prone to oscillations at the intersection frequency around the magnitude peak point. That's the key reason why the SSO phenomenon can happen in an MMC-HVDC system for wind farm integration. However, it should be pointed out that the intersection doesn't always occur, which depends on many factors such as the wind farm output power, control strategies and controller parameters of both the wind power inverter and WFMMC, etc.

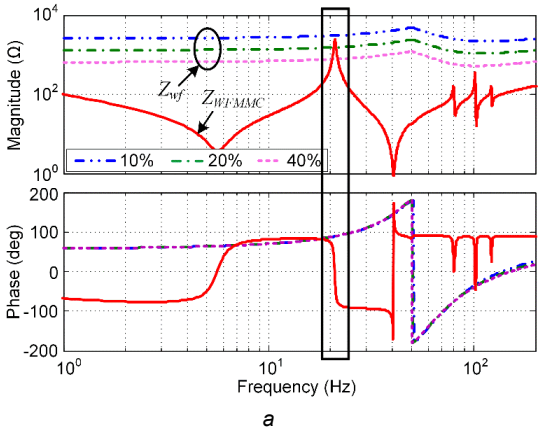

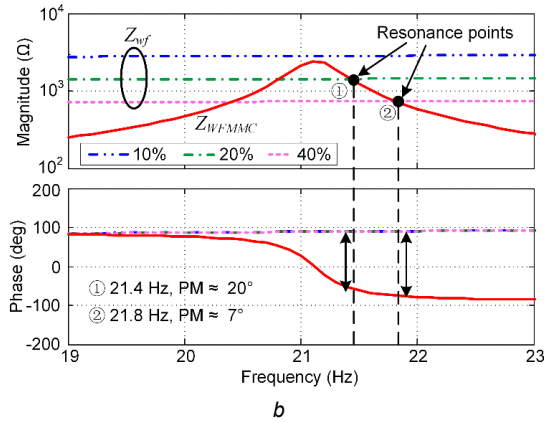

b

Fig. 4. *AC-side impedance characteristics of the WFMMC and wind farm*
a Overall view
b Zoom in view.

5.2. *Influence factors analysis based on Nyquist plots*

According to the instability mechanism analysis above, the key reason of the SSO in the MMC-HVDC system for wind farms is the weak damping (i.e., very low phase margin) at the low-frequency intersection point of the magnitude-frequency characteristics of the WFMMC and wind farm impedances. Besides the main circuit parameters, the controller parameters and output power level have also great influence on the stability of the interconnected system. Therefore, it is important to understand how these factors influence the stability of the interconnected system so as to guide the system design. The impedance-based Nyquist stability criterion is applied to examine the influence factors in this section.

First of all, the controller parameters of the WFMMC and the wind power inverter are designed separately from a single converter perspective, as presented in Table 1, with which the WFMMC and the wind farm can operate stably even under the rated power condition when they are connected to the ideal load and ac grid, respectively. Then, the stability of the interconnected system is analyzed to understand how the interactions happen between the wind farm and WFMMC by changing the related parameters and meanwhile keeping the other parameters unchanged.

Table 1 Basic controller parameters

Controller Parameters			Values
WFMMC	AC voltage controller	K_{pv}	1
		T_{iv}	0.1 s
Wind power inverter	Current controller	K_{pi}	0.02
		T_{ii}	0.005 s
	PLL controller	K_{pp}	0.13
		T_{ip}	0.05 s

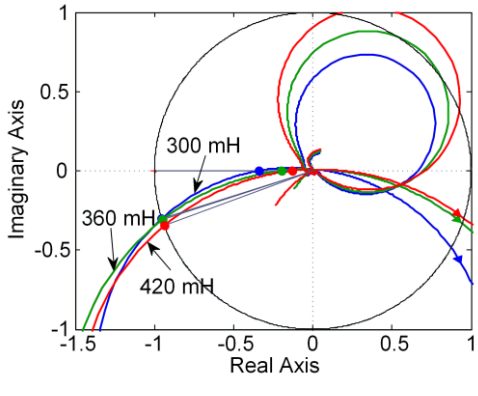

a

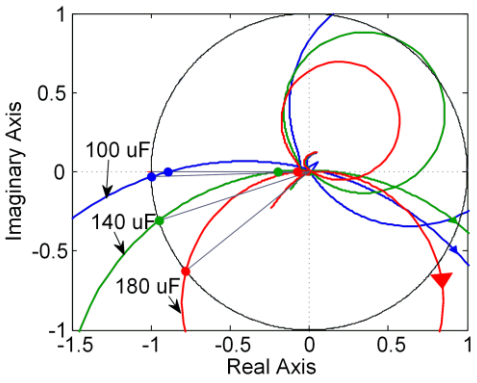

b

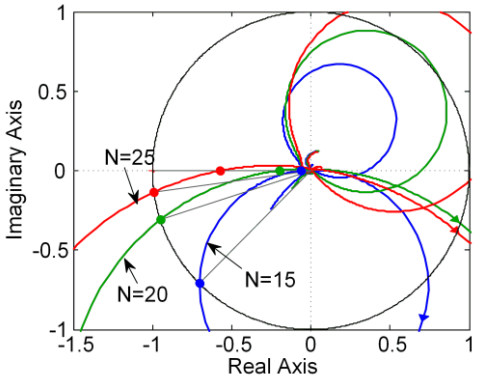

c

Fig. 5. *Impact of the main circuit parameters of the WFMMC on the stability of the interconnected system*
a Arm inductance
b SM capacitance
c SM number per arm

5.2.1 Impact of the main circuit parameters of the WFMMC: Fig. 5 demonstrates the impact of the main circuit parameters of the WFMMC on the stability of the interconnected system seen from the impedance-based Nyquist plots. It can be seen from Fig. 5*a* that the stability margin of the interconnected system becomes large as the arm inductance increases. In addition, the arm equivalent capacitance C_{arm}, which depends on the SM capacitance C_{SM} and SM number N per arm, is another key factor that affects the resonance characteristics of the MMC impedance. The larger the SM capacitance or the fewer the SM number per arm is, the larger the stability margin of the interconnected system is, as shown in Fig. 5*b* and Fig. 5*c*, respectively. For instance, the phase margin of the interconnected system is approximately 2 ° at the frequency of 28 Hz if the SM capacitance is 100 μF, which can be identified by Fig. 5*b*. Moreover, it is worth noting that in a practical application, the main circuit parameters of the MMC are generally designed according to some certain selection principles [25] which, however, haven't considered the impacts on the stability of the interconnected system. Therefore, the analysis results in this paper can provide reference for the system design on the basis of the existing selection principles in order to enhance the stability of the interconnected system.

5.2.2 Impact of the ac voltage controller parameters of the WFMMC: The impact of the ac voltage controller parameters of the WFMMC on the stability of the interconnected system can be examined in a similar way. It can

be concluded that the smaller the proportional gain of the ac voltage controller is, the more unstable the interconnected system becomes. That's because the low-frequency resonance peak of the WFMMC impedance with a smaller proportional gain of the ac voltage controller is more prone to intersecting with the wind farm impedance.

5.2.3 Impact of the controller parameters of the wind power inverter: In a similar way, the impact of the controller parameters of the wind power inverter, including the current controller and PLL controller, on the stability of the interconnected system can also be checked. It is concluded that the larger proportional gain of the current controller and/or the smaller proportional gain of the PLL controller is conducive to the stability of the interconnected system. Moreover, the integral gains of both the current controller and PLL controller have less impact on the stability of the interconnected system.

5.2.4 Impact of the output power level of wind farm: The output power level of the wind farm has a significant impact on the stability of the interconnected system. As illustrated in Fig. 4 seen from an impedance characteristic perspective, it can be observed that the stability margin of the interconnected system decreases as the wind farm output power increases. More seriously, the stability margin of the interconnected system is less than zero, resulting in instability.

5.3. Stabilization control method

According to the instability mechanism analysis in this paper, it is concluded that the low-frequency resonance peak in the WFMMC impedance is the key reason why the SSO can occur in the MMC-HVDC connected wind farms. Therefore, the SSO can be eliminated by reducing the low-frequency resonance peak so as to avoid intersections between the magnitude-frequency characteristics of the wind farm and WFMMC impedances. A virtual arm resistance control method, which is implemented by introducing the circulating current negative feedback control based on a proportional regulator, is proposed to suppress the SSO in the MMC-HVDC based wind farms, as shown in Fig. 6*a*, where the modified modulation voltage v_{cref} is added to the original fundamental modulation voltage. The proportional gain R_a essentially plays a role of a virtual arm resistance. The circulating current reference is $i_{cx}^{*} = P/3/V_{dc}$, where P is the wind farm output active power.

Fig. 6*b* presents the ac-side impedance characteristics of the MMC with the virtual arm resistance control (where R_a=20), which are measured in the simulation. It can be seen that the low-frequency resonance peak is well suppressed so that intersections between the magnitude-frequency characteristics of the wind farm and WFMMC impedances can be avoided, which indicates that the stability of the interconnected system can be guaranteed.

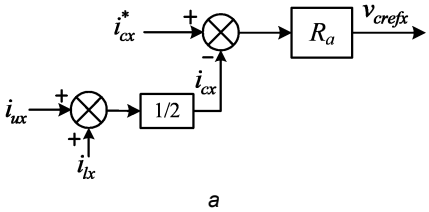

a

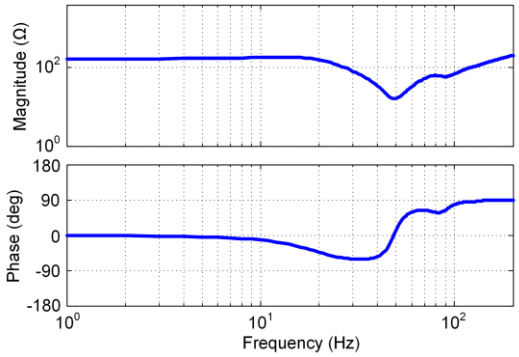

b

Fig. 6. *Virtual arm resistance control*
a Diagram of the virtual arm resistance control
b AC-side impedance characteristics of the MMC with the virtual arm resistance control

6. Simulation results and on-site recorded waveforms

6.1. Simulation results

A time-domain simulation model of the interconnected system (as presented in Fig. 1*b*) is built in MATLAB/Simulink to validate the theoretical analysis. The electrical and controller parameters are the same as those in the frequency-domain analysis above. Fig. 7*a* shows the simulated results of the interconnected system with the basic parameters under 20% of the rated power condition, where the waveforms from top to bottom are three-phase ac phase voltages and currents at PCC, three-phase upper arm currents of WFMMC, dc-side positive- and negative-pole currents and voltages (similarly hereinafter). As can be seen, the interconnected system is marginally stable with slight oscillations, where the dominant oscillation frequency is 22 Hz in the ac-side and 28 Hz in the dc-side which can be identified by the FFT analysis. The simulated results confirm the frequency-domain analysis in Fig. 4 where the insufficient phase margin and oscillation frequency have been well predicted.

Fig. 7*b* presents the simulated results of the interconnected system under 20% of the rated power condition, where the proportional gain of the current controller of the wind power inverter is reduced to 0.008 and the other parameters remain unchanged. It is seen that the interconnected system becomes more seriously oscillatory, which is due to the less phase margin caused by the smaller proportional gain of the current controller. The simulated results are consistent with the theoretical analysis in the previous subsection.

Fig. 7*c* shows the simulated results of the interconnected system with virtual arm resistance control under 40% of the rated power condition. It can be observed that the interconnected system is stable without oscillations in the voltages and currents even under high output power level, which validates the proposed stabilization control method.

6.2. On-site recorded waveforms

In order to further confirm the theoretical analysis in this paper, the on-site recorded waveforms in a real MMC-HVDC project for wind farm integration in China are demonstrated in this paper. In the real system, when the wind farm output power is low, the interconnected system is stable. However, as the wind farm output power increases,

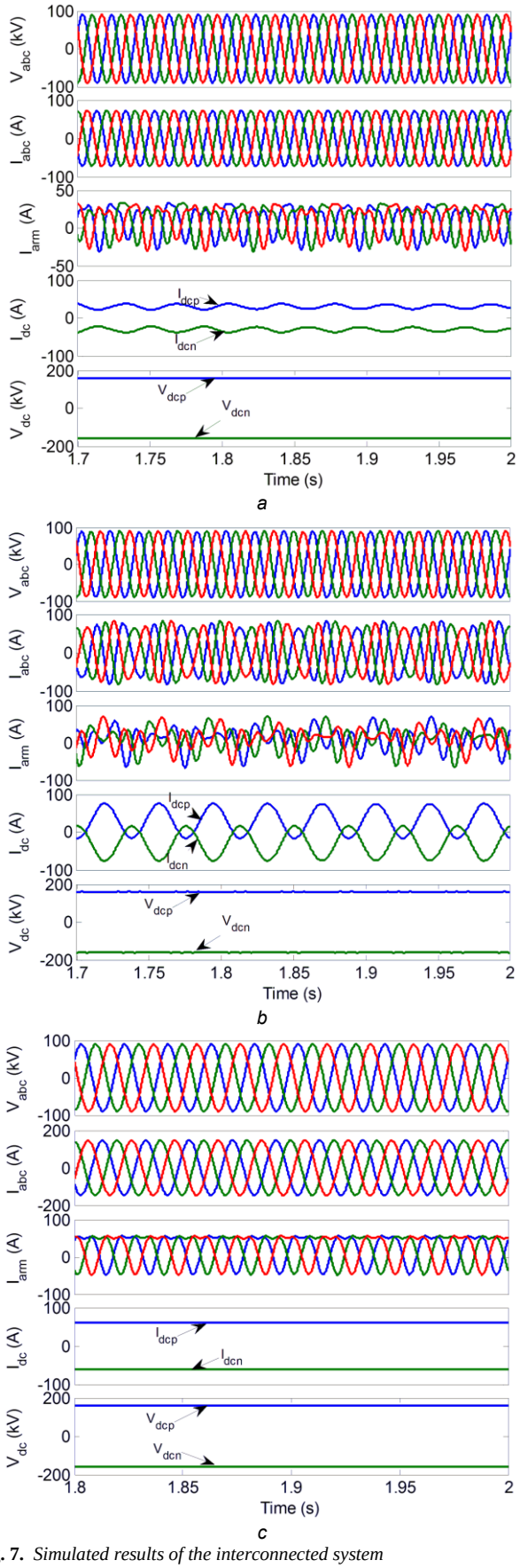

Fig. 7. *Simulated results of the interconnected system*
a With the basic parameters under 20% of the rated power condition
b With the reduced proportional gain of the current controller of the wind power inverter under 20% of the rated power condition
c With the virtual arm resistance control under 40% of the rated power condition

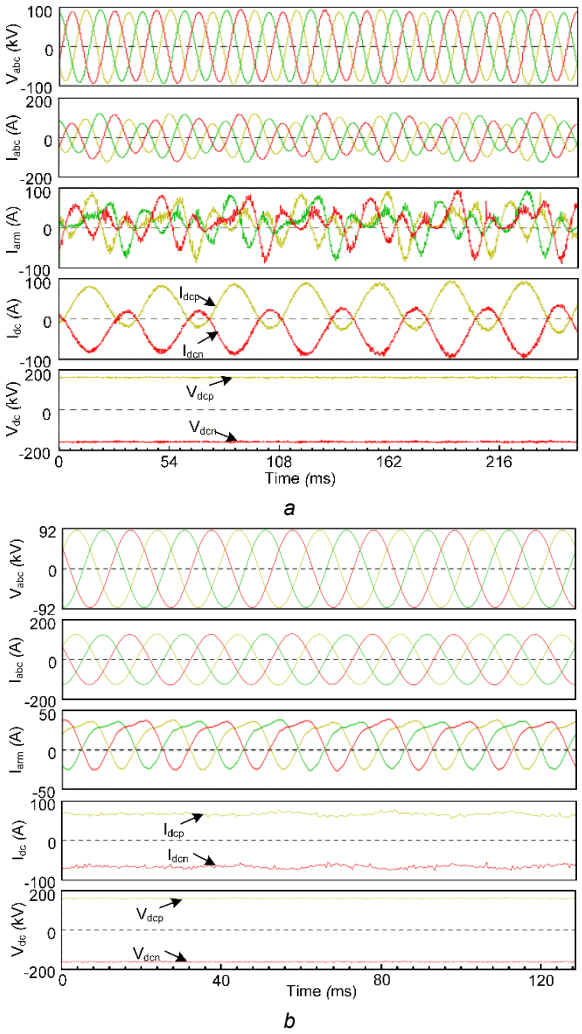

Fig. 8. *On-site recorded waveforms of the real MMC-HVDC system for wind farm integration*
a Without stabilization control under 20% of the rated power condition
b With stabilization control under 40% of the rated power condition

the SSO phenomenon has gradually become obvious, as shown in Fig. 8*a*, where the wind farm output power is approximately 20% of the rated power. As can be seen, there is an obvious SSO in the ac- and dc-side currents, and the dominant oscillation frequency is approximately 21 Hz in the ac-side and 29 Hz in the dc-side, which matches with the analysis in the previous section. However, when the wind farm output power further increases, the MMC-HVDC system is shut down by its protection system, leading to the outage of the wind farm.

Fig. 8*b* presents the on-site recorded stable waveforms of the interconnected system under 40% of the rated power condition, where the virtual arm resistance control is enabled. It can be seen that the interconnected system is stable even under high output power condition, which further confirms the analysis in this paper.

7. Conclusion

This paper discusses the interaction stability of wind farm integration through MMC-HVDC transmission systems. The results indicate that the inherent low-frequency resonance peak in the ac-side small-signal impedance of the WFMMC is identified to be the critical reason why the SSO phenomena occur in the MMC-HVDC connected wind

farms. In general, the interconnected system lacks sufficient phase margin if no additional damping has been provided to the WFMMC, due to its small arm resistance. Furthermore, the influence factors on the stability of the interconnected system are examined, including main circuit parameters, controller parameters, and output power level. A stabilization control method for suppressing the SSO in the MMC-HVDC based wind farms is also proposed. The theoretical analysis and stabilization control method have been validated by both the time-domain simulation results and on-site recorded waveforms in a real MMC-HVDC system for wind farm integration in China.

8. Acknowledgments

This work was partly supported by the National Key Research and Development Program under Grant 2016YFB0900901 and by the ERCIM 'Alain Bensoussan' Fellowship Programme.

9. References

1 Chen, Z., Blaabjerg, F.: 'Wind farm-a power source in future power systems', *Renew. Sustain. Energy Reviews*, 2009, 13, (6), pp. 1288-1300

2 Bresesti, P., Kling, W.L., Hendriks, R.L., Vailati, R.: 'HVDC connection of offshore wind farms to the transmission system', *IEEE Trans. Energy Conver.*, 2007, 22, (1), pp. 37-43

3 Alvarez, A.E., Bianchi, F., Ferre, A.J., Gross, G., Bellmunt, O.G.: 'Voltage control of multiterminal VSC-HVDC transmission systems for offshore wind power plants: design and implementation in a scaled platform', *IEEE Trans. Ind. Electron.*, 2013, 60, (6), pp. 2381-2391

4 Perez, M.A., Bernet, S., Rodriguez, J., Kouro, S., Lizana, R.: 'Circuit topologies, modeling, control schemes, and applications of modular multilevel converter', *IEEE Trans. Power Electron.*, 2015, 30, (1), pp. 4-17

5 Wang, C., Hao, Q., Ooi, B.T.: 'Reduction of low-frequency harmonics in modular multilevel converters (MMCs) by harmonic function analysis', *IET Gener. Transm. Distrib.*, 2014, 8, (2), pp. 328-338

6 Harnefors, L., Antonopoulos, A., Norrga, S., Ängquist, L., Nee, H.P.: 'Dynamic analysis of modular multilevel converters', *IEEE Trans. Ind. Electron.*, 2013, 60, (7), pp. 2526-2537

7 Wang, C., Ooi, B.T.: 'Incorporating deadbeat and low-frequency harmonic elimination in modular multilevel converters', *IET Gener. Transm. Distrib.*, 2015, 9, (4), pp. 369-378

8 Chen, Q., Lyu, J., Li, R., Cai, X.: 'Impedance modeling of modular multilevel converter based on harmonic state space', *Proc. IEEE COMPEL*, Trondheim, Norway, 2016, pp. 1-5.

9 Lv, J., Dong, P., Shi, G., Cai, X., Rao, H., Chen, J.: 'Subsynchronous oscillation of large DFIG-based wind farms integration through MMC-based HVDC', *Proc. Int. Conf. Power Syst. Tech.*, Chengdu, China, 2014, pp. 2401-2408

10 Lü, J., Dong, P., Shi, G., Cai, X., Li, X.: 'Subsynchronous oscillation and its mitigation of MMC-based HVDC with large doubly-fed induction generator-based wind farm integration', *Proceedings of the CSEE*, 2015, 35, (19), pp. 4852-4860

11 Lyu, J., Cai, X., Molinas, M.: 'Frequency domain stability analysis of MMC-based HVdc for wind farm integration', *IEEE J. Emerg. Sel. Topics Power Electron.*, 2016, 4, (1), pp. 141-151

12 Lyu J., Cai, X.: 'Impact of controller parameters on stability of MMC-based HVDC systems for offshore wind farms', *Int. Conf. Renew. Power Gen.*, Beijing, China, 2015, pp. 1-6

13 Lyu, J., Molinas, M., Cai, X.: 'Stabilization control methods for enhancing the stability of wind farm integration via an MMC-based HVDC system', *Proc. IEEE CPE-POWERENG*, Cadiz, Spain, 2017, pp. 324-329

14 Amin, M., Ardal, A., Molinas, M.: 'Self-synchronisation of wind farm in MMC-based HVDC system: a stability invertigation', *IEEE Trans. Energy Conver.*, 2017, 32, (2), pp. 458-470

15 Zhang, S., Jiang, S., Lu, X., Ge, B., Peng, F.Z.: 'Resonance issues and damping techniques for grid-connected inverters with long transmission cable', *IEEE Trans. Power Electron.*, 2014, 29, (1), pp. 110-120

16 Bradt, M., Badrzadeh, B., Camm, E., Mueller, D., Schoene, J., Siebert, T., Smith, T., Starke, M., Walling, R.: 'Harmonics and resonance issues in wind power plants', *Proc. IEEE Power Energy Society General Meeting*, San Diego, USA, 2011, pp. 1-8

17 Miao, Z.: 'Impedance-model-based SSR analysis for type 3 wind generator and series-compensated network', *IEEE Trans. Energy Conver.*, 2012, 27, (4), pp. 984-991

18 Liu H., Sun, J.: 'Voltage stability and control of offshore wind farms with ac collection and HVDC transmission', *IEEE J. Emerg. Sel. Topics Power Electron.*, 2014, 2, (4), pp. 1181-1189

19 Amin M., Molinas, M.: 'Understanding the origin of oscillatory phenomena observed between wind farms and HVdc system', *IEEE J. Emerg. Sel. Topics Power Electron.*, 2017, 5, (1), pp. 378-392

20 Arrillaga, J., Medina, A., Lisboa, M.L.V., Cavia, M.A., Sanchez, P.: 'The harmonic domain. A frame of reference for power system harmonic analysis', *IEEE Trans. Power Syst.*, 1995, 10, (1), pp.433-440

21 Kwon, J., Wang, X., Blaabjerg, F., Bak, C.L., Sularea, V.S., Busca, C.: 'Harmonic interaction analysis in grid-connected converter using harmonic state space (HSS) modeling', *IEEE Trans. Power Electron.*, 2017, 32, (9), pp. 6823-6835

22 Sun, J.: 'Small-signal methods for ac distributed power systems-a review', *IEEE Trans. Power Electron.*, 2009, 24, (11), pp. 2545-2554

23 Cespedes, M., Sun, J.: 'Impedance modeling and analysis of grid-connected voltage-source converters', *IEEE Trans. Power Electron.*, 2014, 29, (3), pp. 1254-1261

24 Sun, J.: 'Impedance-based stability criterion for grid-connected inverters', *IEEE Trans. Power Electron.*, 2011, 26, (11), pp. 3075-3078

25 Bärnklau, H., Gensior, A., Bernet, S.: 'Submodule capacitor dimensioning for modular multilevel converters', *IEEE Trans. Ind. Appl.*, 2014, 50, (3), pp. 1915-1923

10. Appendix

The elements of $\mathbf{A}_p$ and $\mathbf{B}_p$ are shown in (A1)~(A5), in which the subscript "h" (h=0,1,2…) of the state variables represents the Fourier coefficient of the hth harmonic of the state variable under steady state, which can be calculated by (18).

$$A_0=\begin{bmatrix} -\frac{R}{L} & -\frac{1}{4L} & -\frac{1}{4L} & \frac{G_v\left(V_{cu0}^{\Sigma}-V_{cl0}^{\Sigma}\right)}{2L}Z_L \\ \frac{1}{2C_{arm}} & 0 & 0 & \frac{1}{4C_{arm}}-\frac{G_v\left(I_{c0}+\frac{I_{g0}}{2}\right)}{C_{arm}}Z_L \\ \frac{1}{2C_{arm}} & 0 & 0 & -\frac{1}{4C_{arm}}+\frac{G_v\left(I_{c0}-\frac{I_{g0}}{2}\right)}{C_{arm}}Z_L \\ 0 & -\frac{1}{2L} & \frac{1}{2L} & -\frac{R}{L}+\frac{G_v\left(V_{cu0}^{\Sigma}+V_{cl0}^{\Sigma}\right)-2}{L}Z_L \end{bmatrix} \quad \text{(A1)}$$

$$A_{\pm1}=\begin{bmatrix} 0 & \frac{me^{\pm j\theta_{m1}}}{8L} & -\frac{me^{\pm j\theta_{m1}}}{8L} & \frac{G_v\left(V_{cu\pm1}^{\Sigma}-V_{cl\pm1}^{\Sigma}\right)}{2L}Z_L \\ -\frac{me^{\pm j\theta_{m1}}}{4C_{arm}} & 0 & 0 & -\frac{me^{\pm j\theta_{m1}}}{8C_{arm}}-\frac{G_v\left(I_{c\pm1}+\frac{I_{g\pm1}}{2}\right)}{C_{arm}}Z_L \\ \frac{me^{\pm j\theta_{m1}}}{4C_{arm}} & 0 & 0 & -\frac{me^{\pm j\theta_{m1}}}{8C_{arm}}+\frac{G_v\left(I_{c\pm1}-\frac{I_{g\pm1}}{2}\right)}{C_{arm}}Z_L \\ 0 & \frac{me^{\pm j\theta_{m1}}}{4L} & \frac{me^{\pm j\theta_{m1}}}{4L} & \frac{G_v\left(V_{cu\pm1}^{\Sigma}+V_{cl\pm1}^{\Sigma}\right)}{L}Z_L \end{bmatrix} \quad \text{(A2)}$$

$$A_{\pm h}=\begin{bmatrix} 0 & 0 & 0 & \dfrac{G_v\left(V_{cu\pm h}^{\Sigma}-V_{cl\pm h}^{\Sigma}\right)}{2L}Z_L \\ 0 & 0 & 0 & -\dfrac{G_v\left(I_{c\pm h}+\dfrac{I_{g\pm h}}{2}\right)}{C_{arm}}Z_L \\ 0 & 0 & 0 & \dfrac{G_v\left(I_{c\pm h}-\dfrac{I_{g\pm h}}{2}\right)}{C_{arm}}Z_L \\ 0 & 0 & 0 & \dfrac{G_v\left(V_{cu\pm h}^{\Sigma}+V_{cl\pm h}^{\Sigma}\right)}{L}Z_L \end{bmatrix}\left(h\geq 2\right) \quad \text{(A3)}$$

$$B_0=\left[\frac{G_v\left(V_{cu0}^{\Sigma}-V_{cl0}^{\Sigma}\right)}{2L},-\frac{G_v\left(I_{c0}+\frac{I_{g0}}{2}\right)}{C_{arm}},\frac{G_v\left(I_{c0}-\frac{I_{g0}}{2}\right)}{C_{arm}},\frac{G_v\left(V_{cu0}^{\Sigma}+V_{cl0}^{\Sigma}\right)-2}{L}\right]^T \quad \text{(A4)}$$

$$B_{\pm h}=\left[\frac{G_v\left(V_{cu\pm h}^{\Sigma}-V_{cl\pm h}^{\Sigma}\right)}{2L},-\frac{G_v\left(I_{c\pm h}+\frac{I_{g\pm h}}{2}\right)}{C_{arm}},\frac{G_v\left(I_{c\pm h}-\frac{I_{g\pm h}}{2}\right)}{C_{arm}},\frac{G_v\left(V_{cu\pm h}^{\Sigma}+V_{cl\pm h}^{\Sigma}\right)}{L}\right]^T\left(h\geq 1\right) \quad \text{(A5)}$$